Excitation-scanning hyperspectral video endoscopy: enhancing the light at the end of the tunnel

CRAIG M. BROWNING,[1,2] JOSHUA DEAL,[3,4] SAM MAYES,[1,2] ARSLAN ARSHAD,[1] THOMAS C. RICH,[3,4] AND SILAS J. LEAVESLEY[1,3,4,*] (iD)

[1] *Chemical and Biomolecular Engineering, University of South Alabama, AL 36688, USA*
[2] *Systems Engineering, University of South Alabama, AL 36688, USA*
[3] *Pharmacology, University of South Alabama, AL 36688, USA*
[4] *Center for Lung Biology, University of South Alabama, AL 36688, USA*
[*] *leavesley@southalabama.edu*

Abstract: Colorectal cancer is the 3rd leading cancer for incidence and mortality rates. Positive treatment outcomes have been associated with early detection; however, early stage lesions have limited contrast to surrounding mucosa. A potential technology to enhance early stagise detection is hyperspectral imaging (HSI). While HSI technologies have been previously utilized to detect colorectal cancer *ex vivo* or post-operation, they have been difficult to employ in real-time endoscopy scenarios. Here, we describe an LED-based multifurcated light guide and spectral light source that can provide illumination for spectral imaging at frame rates necessary for video-rate endoscopy. We also present an updated light source optical ray-tracing model that resulted in further optimization and provided a ~10X light transmission increase compared to the initial prototype. Future work will iterate simulation and benchtop testing of the hyperspectral endoscopic system to achieve the goal of video-rate spectral endoscopy.

1. Introduction

The suffix -scopy comes from the Greek word -*skopia* meaning "view, observe" [1]. In modern English the suffix implies use of an instrument, referred to as a "-scope", to examine aspects of the universe. To examine our world (or other worlds) we use a telescope/telescopy, to see the world invisible to the naked eye we use a microscope/microscopy and to see internal cavities of the human body we use endoscopes or bronchoscopes/endoscopy. Endoscopes visualize the upper and lower gastrointestinal (GI) tract for abnormalities such as Barrett's esophagus, diverticulitis and colorectal cancer. Bronchoscopes are used to visualize the first three major branches of the bronchial tract in the lungs to detect and characterize fluid accumulation, asthma, COPD and lung cancer.

Lung and colorectal cancers are among the top three cancers in incidence and mortality rates in the United States [2,3]. Interestingly these high risk cancers occur in organs that we have the ability to access and visualize. The gold standard screening technology is white light endoscopy (WLE) for the GI tract and white light bronchoscopy (WLB) for the bronchial tract. However, early stage lesions may often go undetected during an endoscopic screening [4,5]. Prior studies of colorectal endoscopy effectiveness have documented limitations that include: low contrast of early stage or small lesions compared to the surrounding mucosa and the limited ability to determine the metastatic or invasive potential of lesions [6,7]. Hence, a key limitation in endoscopy is the ability to visualize and accurately classify types of lesions. Miss rates for colorectal lesions may involve an expertise bias factor, where novice gastroenterologists or medical students have shown higher miss rates than experts [8]. Pulmonology studies have demonstrated similar detection limitations when examining the upper airways [9–11]. Newer

modalities have been developed for enhanced visualization of endoscopically-accessible organs including: chromoendoscopy (CE), narrow-band imaging (NBI), autofluorescence imaging (AFI), radial endobronchial ultrasound (R-EBUS) and optical coherence tomography (OCT) [10,12–17]. Unfortunately, newer macroscopic imaging techniques (CE, NBI and AFI) have shown minimal improvements for detection accuracy and exterior scans (R-BUS and OCT) of the peripheral bronchial tree are in the infancy stages of development. Hence, there is a need for improved endoscopic imaging technologies that can provide enhanced contrast between "normal" tissue and abnormalities and determine the composition of those abnormalities (estimation of composition, staging and metastatic potential).

One solution may be to incorporate hyperspectral imaging (HSI) into routine endoscopic screening procedures. Hyperspectral imaging captures a two-dimensional spatial image over a range of wavelengths creating a hyperspectral image cube. Each pixel is a spectrum that can be analyzed to estimate the abundance of respective components in that pixel. Hyperspectral imaging can be implemented over different wavelength ranges using different contrast modalities, including reflectance or fluorescence. The broader utility of hyperspectral imaging has been demonstrated in remote sensing notably through agriculture and archaeology [18–21], food processing [22,23], historical documentation and art preservation [24,25]. Within the medical field, HSI has been exemplified through image guided surgeries and cancer detection [26–29]. Studies that have incorporated spectroscopic techniques, with a focus on HSI, into endoscopy thus far have integrated one of the following: a change in the light path, a separate probe (i.e. Raman) through the endoscope working channel or a hyperspectral camera [30–32]. The latter two approaches are more prevalent in gastroenterology literature. Prior studies have compared the spectral characteristics of healthy and cancerous tissues *in vivo* using a hyperspectral endoscopic setup with narrowband filter wheels [33]. The feasibility of an *in vivo* Raman probe was also investigated by introducing the probe through the working channel of an endoscope for the detection of gastric cancer [34]. Additional studies have shown that reflectance spectral data in the visible [35] and infrared [36] ranges can be used to characterize healthy and cancerous gastric tissues. Finally, preliminary *ex vivo* studies have shown that colorectal tissues may be classified using spectral image data, as referenced to histopathology [37]**.** However, there are four key aspects of prior studies that point to the limitations of current HSI and spectroscopic techniques in endoscopy and the need for further technology development: 1) prior studies have been performed almost exclusively *ex vivo* using resected tissues, 2) the majority of prior studies have utilized reflectance spectroscopic data, 3) single-point measurements, such as with Raman spectroscopy probes, have not been able to visualize large tissue areas as would be needed for real-time screening and 4) snapshot HSI approaches provide spectral information at the price of reduced resolution and loss of signal. While many prior studies indicate an end-goal of developing real-time endoscopic imaging systems, the majority of prior work has been limited to *ex vivo* preparations, likely due to a combination of challenges including those associated with obtaining IRB and regulatory approval, difficulties associated with implementing an integrated real-time HSI endoscope system, and the limited signal strength available if the HSI approach is implemented at video-rate speeds [35–37]. Correspondingly, most prior HSI studies have utilized only reflectance spectral data, as the signal strength is higher than fluorescence and much higher than Raman modalities [33,35–37]. However, there is likely valuable information contained in fluorescence spectral data and an approach that could sample both reflectance and fluorescence modalities could provide enhanced visualization and diagnostic capabilities. Normal and abnormal tissues are expected to present distinct spectral differences due to changes such as reflectance vascular density or fluorescence metabolism markers [12,38–43]. Hence, using a mixture of reflectance and fluorescence spectral signals could provide additional contrast needed to enhance visual differences between tissue types and improve visualization. A subsection of endoscopic spectroscopy studies involve single-point measurements including diffuse optical and

Raman spectroscopy which can provide detailed molecular composition, but only of a single point in the tissue [34]. The main limitation of these techniques is the need to sample the tissue on a point-by-point basis, which may lead to long procedure times. Lastly, many prior studies implementing HSI into endoscopy have used the snapshot technique to acquire a spectral image stack [35–37]. However, this approach may be limited in that it requires a trade-off between reduced spatial and spectral resolution [44]. Hence, challenges remain in developing a viable endoscopic HSI platform, but regardless of the approach, a new HSI technology needs to provide a comparable field of view (FOV) to the gold standard WLE, *in vivo* capabilities and video-rate image data acquisition, preferably with the option to detect mixed modalities (reflectance and fluorescence).

We have previously reported on the use of excitation-scanning hyperspectral imaging to discriminate fluorescent markers (nuclei, green fluorescent proteins and tissue autofluorescence) in mice lung tissue models [45–49]. Our previous microscope-based approaches allowed collection of the entire fluorescence emission above a cut-off wavelength for each excitation wavelength band providing improved photon statistics and therefore a higher signal-to-noise ratio, when compared to similarly configured emission-scanning approaches. Furthermore, fluorescence microscopy image acquisition speeds were able to be increased by a factor of ~10X for excitation-scanning approaches compared to emission-scanning. However, a limitation of these prior implementations is that they used an array of thin film tunable filters to provide spectral excitation and the mechanical tuning required 50-200 ms to switch between wavelengths. Hence, while prior microscope-based systems have shown great potential for fixed and/or single field of view images, they have not been capable of acquiring video-rate hyperspectral image data. To develop an excitation-scanning hyperspectral imaging system for endoscopic use, wavelength switch times need to be much shorter – on the order of ~100 μs. Here, we present an imaging approach that utilizes wavelength-specific LEDs as the spectral excitation source. Similar approaches found in literature for LED-based HSI systems were designed for diffuse, macroscopic reflectance imaging which has minimal ability to couple to an illumination fiber of an endoscope [50,51]. Here, we developed a novel multifurcated solid light guide to combine optical output from many LEDs and couple the output into an endoscope illumination fiber. The electronic switching of LEDs is on the order of 100 ns. In this manuscript, we present the initial specifications for a proof-of-concept LED-based spectral light source for endoscopy, initial benchtop testing and computational simulations to optimize the light path. Results demonstrate that excitation-scanning hyperspectral imaging for video-rate endoscopy is possible. A resulting system from this work could provide spectral endoscopy screening for enhanced visualization of colorectal cancers.

2.　Methods

Here, we present an iterative, systems-based methodology for developing the prototype spectral endoscope system that includes: 1) optical simulations of a proof-of-concept multi-branched solid light guide, 2) benchtop testing a LED-based spectral light source with the fabricated proof-of-concept solid light guide for endoscopic settings, and 3) revised optical simulations for further improving the solid light guide that lead to an optimized design for the spectral illumination assembly. The initial iteration of a multi-branched solid light guide is referred to as the alpha light guide design phase and the revised iteration of the light guide is referred to as the beta light guide design phase. Parametric optical simulations for the beta light guide are further divided into 3 tiers: Tier 1 – single lightpipe parameters, Tier 2 – combining lightpipe branches and Tier 3 – optimized multi-furcated solid light guide designs. For this manuscript a light guide refers to a combination of lightpipes. A key element of the system is an array of wavelength-specific LEDs to provide the spectral illumination to the endoscope. Herein, we use

the term λLED to denote wavelength-specific LEDs and as a reminder that many narrowband (typically 20 nm FWHM) light sources are utilized for spectral illumination.

2.1. *Proof of concept λLED -based spectral light source*

2.1.1. Alpha light guide design

To assess the feasibility of a spectral endoscopic light source based upon multiple λLED sources combined through a multifurcated solid light guide, we first developed computational models of solid light guides. We then manufactured a proof-of-concept alpha prototype solid light guide from the simulation results and performed bench testing for optical efficacy. We then constructed a spectral light source utilizing the alpha prototype solid light guide and coupled the spectral light source to an endoscope. All light path modeling was simulated using Monte Carlo-based optical ray tracing software (TracePro, Lambda Research Co.). To assess repeatability of the ray tracing, an initial simulation was performed 5 times with 1,000,000 rays traced. The output irradiance of the system was measured and found no variation between subsequent ray traces. This was deemed a statistically sufficient number of rays to accurately model the simulations for this study. To verify that 1,000,000 rays were accurate, we also performed simulations with 100,000 and 5,000,000 rays and found that the output irradiance varied by less than 0.05%. The materials and parameters selected for the light path components of the alpha design are summarized in Table 1.

Table 1. Key parameters used for ray trace simulations of the alpha phase multi-furcated light guide

Light Source: Cree LED C503B-BAS/BAN/GAS/GAN	Wavelength (nm)	527
	Luminous Intensity (cd)	30
	Radiated Power (mW)	10
	Full Viewing Angle (°)	15
	Rays Traced	1,000,000
Optics: Light Guide	Material/Refractive Index	Plexiglass/1.49
	Distance from Source (mm)	2
Detector/Interrogation Plane/Irradiance Map	Diameter (mm)	50
	Distance from Guide (mm)	50

The alpha light guide computational models simulated a LED light source (Cree LED C503B-GAS, Cree Inc.) with a narrow (15° full angle) angular illumination distribution. Light was directed through a solid lightpipe or light guide using material properties with a refractive index of 1.49 (Plexiglass). The emitted flux from the output of the light guide was measured at the exiting face and with an interrogation plane perpendicular to the light guide output. Percent transmission through the light guide (e.g. optical efficiency) and the illumination distribution were calculated.

The alpha light guide computational models tested individual geometric parameters including lightpipe diameter, arc length of lightpipe curvature (as a function of radius and angle of the curvature), branching structures and spacing between distal branches of a light guide. The geometries for the alpha phase design were rendered using CAD (Autodesk Inventor, Autodesk Inc.) and imported to TracePro. A circular cross-section was used for all lightpipe and light guide geometries. Transmission throughput was calculated by dividing the output flux from the common end of the light guide by the input flux to the light guide branches from the λLED. From these tests and data, a final alpha phase 16 branched solid light guide was designed in CAD (Autodesk Inventor, Autodesk Inc.) then imported into TracePro for final optical simulations (see Fig. 1). A ray trace was performed for each input branch to determine transmission throughput and

loss per branch. This design was used to assess the initial feasibility of utilizing a multifurcated light guide for a λLED -based spectral light source.
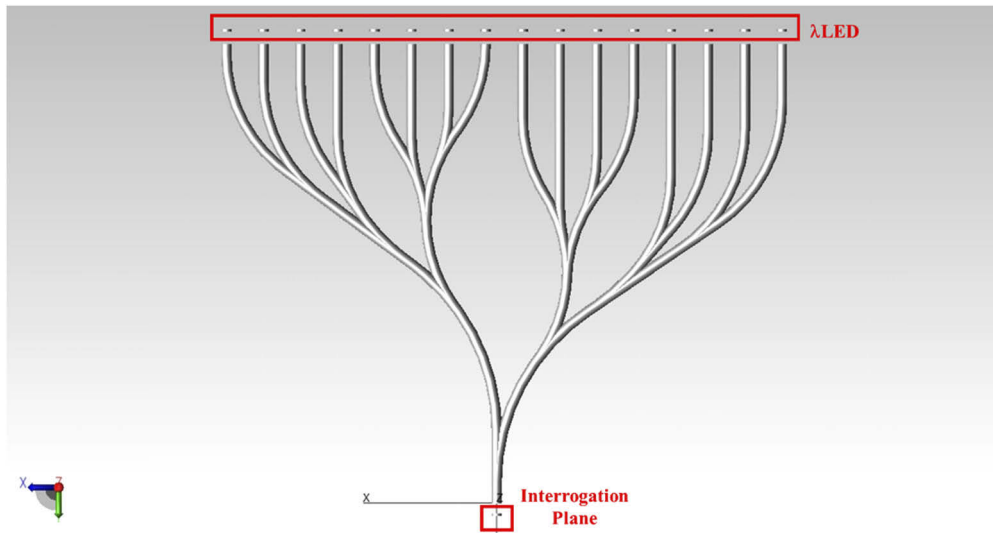

Fig. 1. Rendering of the alpha phase multi-branched solid light guide in ray tracing software for simulated optical analysis. The small disks at the top of the rendering modeled the illumination from each LED. The small disk at the bottom of the model is the exit surface, interrogation plane.

2.1.2. Spectral endoscopic light source

The alpha light guide design was fabricated by injection molding of optical grade acrylic to combine an array of wavelength-specific LEDs (λLEDs) to a common output. High-powered surface mount λLEDs (SMBBXXX-XXXX-XXX, Marubeni Co.) were implemented with an average (full) viewing angle of 22° and power outputs ranging from 120 to 750 mW, depending on wavelength. A custom printed circuit board (PCB) was designed (Pad2Pad, Pad2Pad Inc.) to align λLEDs with distal light guide branches. A coupler from a commercial endoscopic light source (Olympus CLK-4, Olympus Medical Systems Corp.) was integrated to align the optical, proximal output of the light guide with the illumination input of a compatible fiber scope (Olympus CF-P20S). A second custom PCB employed current drivers (RCD-XX-X.XX, RECOM Power) to independently control intensity and cycling of each λLED. Other electronic components included a 15V power converter and a relay switch to supply standard facility power to the current controller PCB. The electrical interface is further detailed using a system architecture internal block diagram (IBD) (Fig. 2). Additional mechanical components included an internal fan for LED heat dissipation and an air pump for potential tissue/cavity inflation scenarios through the scope. The multifurcated solid light guide was fabricated to be approximately 9" length by 12" width, and was housed within the complete spectral light source rackmount (25" L x 19" W x 7" H). These system details can be seen in **Fig. 3.**

The IBD presents the flow of power to illuminate the λLEDs and the signals used to control the intensity and cycle of illumination. The perimeter in Fig. 2 defines the black box boundaries of the electrical subsystem with inputs on the left and outputs on the right. The electrical and optical subsystems are prioritized to emphasize the novel features and techniques developed for the hyperspectral endoscope system. The completed spectral light source was coupled with a retired Olympus CF-P20S endoscope for proof-of-concept benchtop testing (Fig. 3).
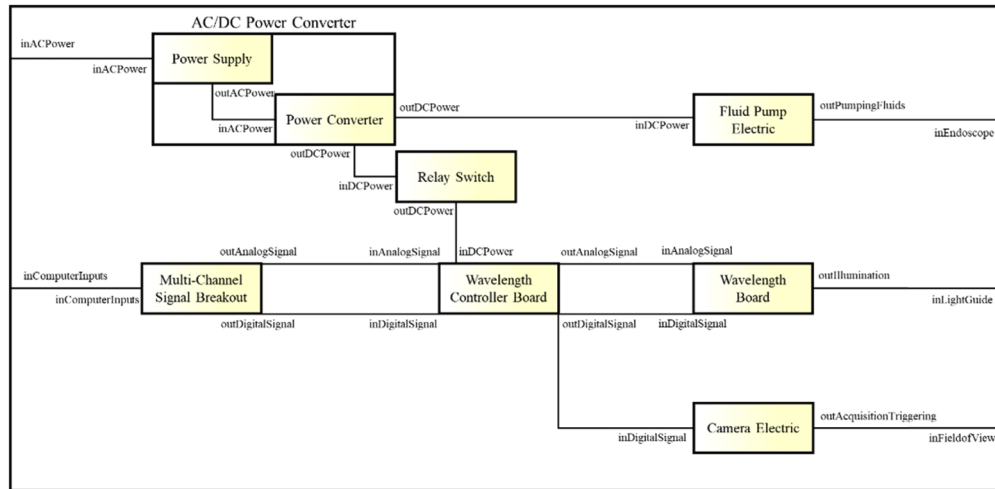
Fig. 2. A systems architecture internal block diagram view of the electric interface of the hyperspectral endoscopic light source, specifically for the alpha design proof-of-concept light source.
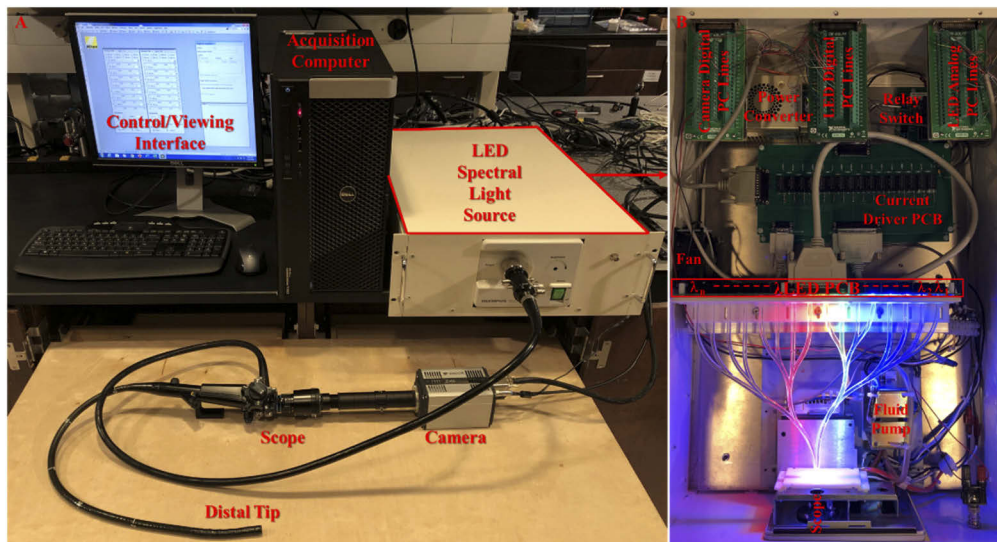

Fig. 3. Complete proof-of-concept spectral endoscope system overview. (A) System photograph with labels for the major subsystems: computer, spectral light source, scope and camera. (B) Top view of the spectral light source with labels for the key electronic components previously described in Fig. 2. The spectral light source optical pathway combines illumination from the λLEDs into a single output using a novel multi-branched solid light guide. The output is then coupled to the illumination fiber of a standard endoscope.

2.1.3. Benchtop testing alpha hyperspectral endoscopic system

Benchtop testing consisted of determining optical power throughput and testing image quality in tissue models. The transmission intensity was measured using a spectrometer (QE65000, Ocean Optics) and integrating sphere (4P-GPS-030-SF, Labsphere) calibrated to a NIST-traceable response using a standardized light source (LS-1-CAL, Ocean Optics). All measurements were

acquired by averaging 10 scans of the spectrometer. Irradiance data was collected from: 1) the raw λLED, 2) the output of the light guide coupled to the λLED and 3) the output of the endoscope coupled to the light guide and λLED. Measurements were acquired over a range of currents supplied to the λLED, as regulated using an analog reference voltage signal supplied by a National Instruments PCI-6723 card to the current drivers (the Multi-Channel Signal Breakout of Fig. 2). The current drivers supplied current to each λLED with an output that was inversely proportional to the analog reference voltage supplied to the driver (reference voltage ranged from 5V to 0.5V in increments of 0.5V). The maximum power output from the light guide and from the endoscope were divided by the maximum raw λLED power to calculate the % transmission through each stage of the system. The range of power measurements was used to provide a correlation between power output and analog reference voltage inputs to ensure a flat spectral output (i.e. even illumination intensity across all λLEDs).

2.1.4.　Preliminary tissue image testing

Images were acquired using an external camera (Zyla 5.5, Andor) and relay lens assembly coupled at the endoscope eyepiece. Discarded swine tissues were obtained from the University of South Alabama Vivarium, following IACUC-approved procedures associated with medical student and surgical fellow training. Samples were rinsed thoroughly with phosphate buffered saline (PBS) and attached to a mechanical holder such that the proximal end of each tissue was clamped shut and the distal end was open to allow endoscope insertion. The endoscope was inserted and sample images and video feed were acquired at several locations. A range of acquisition times and illumination intensities were compared to determine optimal settings.

2.2.　*Optimized ray trace modeling*

Benchtop testing and tissue imaging results from the alpha phase light source (results in Section 3.2) indicated feasibility of a multi-branched light guide for spectral illumination, however, further investigation for optimal geometric design of the light guide was needed. Therefore, a second iteration (beta phase) of computational ray trace models was developed to determine an optimal multi-branched light guide design. Optical material and geometric parameters were updated to better match the physical properties of the high-power λLEDs in benchtop testing and from the knowledge of the alpha light guide simulations (Table 2).

Table 2. Key parameters used for ray trace simulations of the beta phase multifurcated light guide

	Wavelength (nm)	525
	Luminous Intensity (cd)	270
Light Source: Marubeni LED SMB1N-525-02	Radiated Power (mW)	230
	Full Viewing Angle (°)	22
	Rays Traced	100,000
Optics: Light Guide	Material/Refractive Index	Acrylic/1.49
	Distance from Source (mm)	2
	Surface Property	Perfect Absorber
Detector/Interrogation Plane/Irradiance Map	Diameter (mm)	5
	Distance from Guide (mm)	2

The optical parameters of the high-power λLEDs, acquired for the proof-of-concept light source, were imported from the manufacturer specifications sheet using the Surface Source Property Editor in TracePro for the ray tracing analysis. The model repeatability analysis mentioned above was conducted to determine the number of rays required to yield repeatable model results in efficient time periods. Tracing 100,000 rays yielded sufficient repeatable results

(repeatability fluctuation of ≤0.05%), while allowing for relatively rapid computational times when iterating through geometric parameter values. The light guide material was adjusted to match the fabricated alpha light guide. The size and placement of the interrogation plane was adjusted to more accurately predict the coupling efficiency with an endoscopic illumination fiber. Mechanical, non-optical components were not included in the ray trace simulation. In addition, the CLK-4 coupler was not included in the ray trace simulation, as it is part of the detection pathway and the ray trace simulation was performed to optimize the illumination optics. A parametric simulation process was used that varied one or more geometric variables independently (i.e. arc length or wavelength illuminated). A separate iteration of the model was performed for each value of each independent variable. The output of each iteration was saved in the form of an irradiance map of the interrogation plane and % transmission of the light guide. Irradiance maps were normalized to the emitted flux of the LED. This process was repeated for every value of the independent variable for every independent variable altered.

Table 3. Manufacturer-supplied properties of the high-powered surface mount LEDs used in the beta phase simulations and in the alpha phase prototype. Physical light sources were used in the prototype spectral light source (Fig. 3) and digital light sources, by importing the optical properties to TracePro for simulation loops (first column). The tabulated data were used to determine the theoretical % transmission required at each wavelength of LED to achieve a specified power output. As an example, if the desired power output is specified as 10 mW, the 395 nm LED chip can achieve this power output even if the transmission of the spectral system is as low as 1%, while the 590 nm LED (a lower output chip than 395 nm chip) would require 8% transmission to achieve an optical power output of 10 mW.

Macro List Identifier	Marubeni LEDs	Forward Current (mA)	Radiated Power @ Current Forward (mW)	Desired Power Output (mW)						
				10	20	30	40	50	60	70
1	SMB1N-365V-02	500	500	2%	4%	6%	8%	10%	12%	14%
2	SMB1N-375V-02	500	560	2%	4%	5%	7%	9%	11%	13%
3	SMB1N-395V-02	500	750	1%	3%	4%	5%	7%	8%	9%
4	SMB1N-405V-02	500	710	1%	3%	4%	6%	7%	8%	10%
5	SMB1N-420H-02	350	420	2%	5%	7%	10%	12%	14%	17%
6	SMB1N-D450-02	350	480	2%	4%	6%	8%	10%	13%	15%
7	SMB1N-D470-02	350	470	2%	4%	6%	9%	11%	13%	15%
8	SMB1N-490H-02	350	240	4%	8%	13%	17%	21%	25%	29%
9	SMB1N-515V-02	350	250	4%	8%	12%	16%	20%	24%	28%
10	SMB1N-D520-02	350	250	4%	8%	12%	16%	20%	24%	28%
11	SMB1N-525V-02	350	230	4%	9%	13%	17%	22%	26%	30%
12	SMB1N-590-02	350	120	8%	17%	25%	33%	42%	50%	58%
13	SMB1N-620-02	350	190	5%	11%	16%	21%	26%	32%	37%
14	SMB1N-D630-02	350	330	3%	6%	9%	12%	15%	18%	21%
15	SMB1N-D660-02	350	250	4%	8%	12%	16%	20%	24%	28%
16	SMB1N-670D-02	350	290	3%	7%	10%	14%	17%	21%	24%
17	SMB1N-680-02	600	170	6%	12%	18%	24%	29%	35%	41%
18	SMB1N-750-02	800	290	3%	7%	10%	14%	17%	21%	24%
19	SMB1N-810D-02	800	560	2%	4%	5%	7%	9%	11%	13%
20	SMB1N-850D-02	1000	650	2%	3%	5%	6%	8%	9%	11%
21	SMB1N-940D-02	1000	630	2%	3%	5%	6%	8%	10%	11%

Performance requirements of the beta phase model were defined in order to achieve improved physical outcomes over the alpha phase prototype: 1) The endoscopic system as a whole should be capable of providing an optical output of 10 mW at each wavelength band. 2) The optical output of the multifurcated light guide should have a numerical aperture equal to or less than that of the endoscope/bronchoscope illumination fiber to enable efficient optical coupling. 3) The optical output should be stable and the output at each wavelength band should be equal in order to achieve flat spectral illumination. Manufacturer properties for each λLED were tabulated and compared in order to ensure that a flat spectral profile could be achieved for a specified optical illumination power (Table 3).
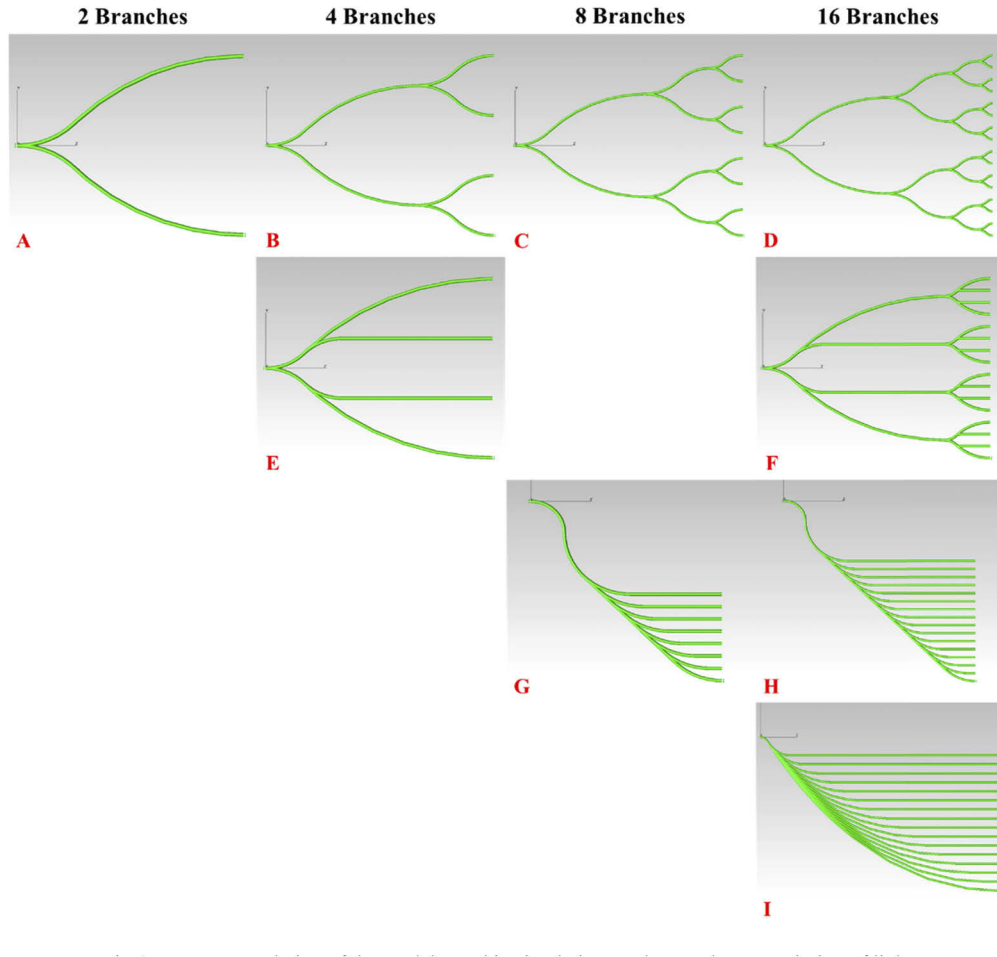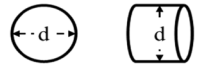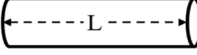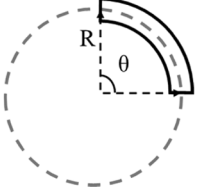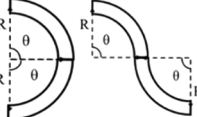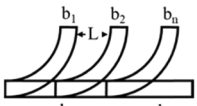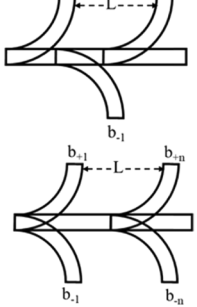

Fig. 4. TracePro rendering of the models used in simulation to observe the transmission of light through a multi-branched solid light guide. The percent transmission of each light guide branch was monitored for the symmetrical model at (A) two branches, (B) four branches, (C) eight branches and (D) sixteen branches. A symmetrical model with a reduced number of merge points at (E) four branches and (F) sixteen branches was also evaluated. In addition, a non-symmetrical geometry that was labeled a "wave shaped" geometry was evaluated for (G) an eight-branch light guide with 90° sweeping angles, (H) a sixteen-branch light guide with 90° sweeping angles and (I) a sixteen-branch light guide with 45° sweeping angles.

The following two sections describe the systematic and parametric evaluation of the beta phase light guide. The first section (Tier 1 & 2) describes simulation of single (unbranched) and dual

(converging two lightpipe branches together) lightpipe geometries. The second section (Tier 3) describes simulation of more complex multi-branched solid light guide models.

2.2.1.   Lightpipe simulations (Tier 1 & 2)

Table 4. Summary of results from the alpha phase multi-branched solid light guide ray tracing modeling. Columns 2 and 3 indicate the independent variables that were iteratively tested over the range of values, respectively. Column 4 provides an illustration of each lightpipe model geometry. Column 5 summarizes the results of each parameter tested.

Parameter	Independent Values	Ind. Value Ranges	Visualization	Results
Lightpipe Diameter	Diameter (mm)	1, 5, 10, 25, 50		92% with 10 mm diameter
Lightpipe Length	Length (mm)	10, 50, 250, 500, 750, 1000		~60% independent of length
Lightpipe Curve	Angle (°) Radius (mm)	30°-180° increments of 15° at 50 mm radius 10-50 increments of 10, 100, 150, 300, 500 at 60° angle		55% max for all θ values above 100 mm radius
Lightpipe Double Curve	Angle (°) Radius (mm)	Same ranges holding the first curve constant at given values iterating on the second curve		The results are the same as the single curve above
Number of Lightpipes	Branches (b_n)	1 Branch - 6 Branches		~20% illumination reduction for each branch increase
Lightpipe Spacing	Length (mm)	Parallel: 10, 15, 20, 40 Staggered: 20 if Adjacent, 10 if Opposite. Mirrored: 20		Spacing has NO effect on the transmission

Tier 1 beta phase models were similar in design to models of the alpha phase light guide, but with updated variables and material properties. Parametric sensitivity studies evaluated effects of lightpipe diameter, length and curvature. Tier 2 beta phase models studied the optical tendencies of two merging lightpipes and evaluated the effects of alternating the spacing between the distal ends of merged lightpipes.

2.2.2.   Multifurcated light guide simulations (Tier 3)

Tier 3 of the ray trace modeling for the beta phase multi-branched solid light guide implemented key findings and optical geometry values from the Tier 1 (single lightpipe curvature) and Tier 2

(merging two lightpipes together) models to create new light guide geometries. The creation of new geometries focused on size of curve (radius and angle), how the branches merged and the final size of the completed model. Four multi-branched solid light guide geometries were rendered and evaluated. The independent variables for these models included the selection of the distal branch of the light guide that was coupled to the λLED and the wavelength of the λLED used. For all of the model geometries, branch one was denoted as the branch at the bottom-right of the viewing window, with branch numbers increasing for every branch above. A range of wavelength bands (LED model numbers and associated optical properties) were evaluated, from 365 nm to 940 nm (Table 3) to observe any changes in transmission between branches and to identify which wavelengths had improved transmission.

A symmetrical design (Fig. 4(D)) was evaluated that combined 16 branches with 4 merge points. The percent transmission was measured after each merge point (the addition of merge points/branches are shown in each row of Fig. 4) and at the final common exit of the light guide in order to assess the location(s) of the greatest loss in transmission. A related design was also evaluated that utilized 2 merge points (Fig. 4(F)). In addition, a "wave shaped" light guide was developed with either 8 or 16 branches, where all branches followed the same path and curved the same direction with arbitrary spacing between each branch (Fig. 4(G-H)). As opposed to the symmetrical designs, the "wave shaped" designs had only one main merge point. An additional "wave shaped" light guide (Fig. 4(I)) was also evaluated that utilized a 45° sweep angle instead of a 90° sweep angle.
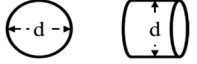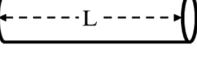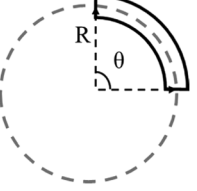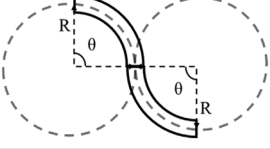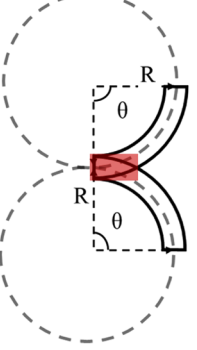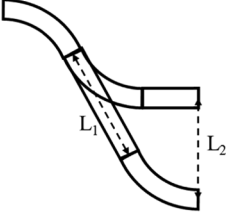
3. Results and discussion

Spectral imaging holds great promise for translation into biomedical screening devices such as endoscopes. Narrow-band imaging and autofluorescence imaging have integrated aspects of spectral specificity into endoscopy but only with one or two bandwidths of illumination. The technology presented here allows many bandwidths of illumination providing a more complete spectral analysis. Resulting spectroscopic data could provide an enhanced visualization of blood flow or metabolic changes in real time. However, studies thus far that have accomplished spectroscopic imaging in endoscopy via snapshot, Raman or filtering techniques cannot provide substantial spatial and spectral resolution or real-time operations. Our prior work with excitation-scanning hyperspectral imaging reduces the emission filtering to increase acquisition speeds (3 s per spectral image using emission-scanning to 300 ms per spectral image using excitation-scanning). This work presents further reduction of illumination filtering by introducing λLEDs to achieve spectral imaging. To our knowledge, this is the first implementation of a multifurcated solid light guide for providing wavelength-band illumination for spectral imaging.

3.1. Alpha light guide models

Here, we describe a parametric modeling approach and subsequent prototyping efforts and proof-of-principle testing to evaluate the potential of a multi-channel light guide for use in spectral imaging applications. The single lightpipe parametric tests and merging lightpipes tests led to the proof-of-concept solid light guide design from Fig. 1. Alpha phase ray trace simulations measured the output flux at the respective surfaces of a given light guide configuration divided by the total power output of the λLED (10 mW) to determine the transmission efficiency. A summary of all alpha phase model results is given in Table 4.

Optical transmission increased with increasing lightpipe diameter ranging from 3-95%. The alpha phase light guide was modeled with a diameter of 5 mm (73% for this diameter) to couple with the high power λLEDs (with a lens diameter of 5 mm on the LED chip) while maintaining a smaller footprint for the light guide. Transmission through increasing lightpipe lengths resulted in a transmission range of 56-60%. Lightpipe curvature (a function of the radius and angle of a circumscribed arc) testing resulted in a transmission increase with increasing arc radius to a

Table 5. Individual geometric parameters simulated in TracePro for iterations of the beta phase multi-branched solid light guide. Columns 2 and 3 indicate the independent variables that were iteratively tested and the range of values tested. Column 4 provides an illustration of each lightpipe geometry. A summary statement of each test's results are provided in Column 5. Tier 1 (single branch lightpipe) models are shown in rows 2-5 and Tier 2 (dual/merged lightpipe) models are shown in rows 6 and 7.

Parameter	Independent Values	Ind. Value Ranges	Visualization	Results
Lightpipe Diameter	Diameter (mm)	2-20 increments of 2, 20-100 increments of 20		86% with 8 mm diameter
Lightpipe Length	Length (mm)	10-100 increments of 10, 100-1000 increments of 100		72% independent of length
Lightpipe Curve	Angle (°) Radius (mm)	15°-90° increments of 15° 10-100 increments of 10, 100-500 increments of 100 at every angle		50% max for all θ values above 100 mm radius
Lightpipe Double Curve	Angle (°) Radius (mm)	Same ranges holding the first curve constant at given values iterating on the second curve		The results are the same as the single curve above
Number of Lightpipes	Angle (°) Radius (mm)	15°-90° increments of 15° 10-100 increments of 10, 100-500 increments of 100 at every angle		35% max for all θ values above 200 mm radius
Lightpipe Spacing	Length (mm)	20-40 increments of 5		Spacing has NO effect on the transmission

maximum transmission of ~55% for arc radii ≥ 100 mm, for all angles tested. Bifurcated lightpipe geometries were also evaluated that consisted of a curved lightpipe (radius: 20 mm angle: 90°) merged with a straight lightpipe. Additional branches were added at equidistant spacing to study the effects of lightpipe furcation, with increasing branch numbers (branch 1 was designated as the branch closest to the common output and branch n as the farthest). Branch positions and spacing were evaluated iteratively. Increasing branches decreased the transmitted light at the output from 66% (for 1 branch) to 7% (for 6 branches). Additional multifurcated models were implemented to evaluate the effects of staggered and mirrored branch geometries, with similar results to the parallel branching model. Spacing between branches presented negligible changes in the transmitted light for all configurations.

The results of the alpha phase ray trace modeling provided a foundation to design an initial proof-of-principle multifurcated light guide. An initial design was developed that combined 16 branches to a common output. The alpha design light guide was constrained to 2 dimensions to simplify injection-mold fabrication. Spacing between the distal branches was set 20 mm apart to create a linear λLED array and allow sufficient spacing between λLEDs for heatsinks and cooling. The curvature of each branch was selected as a compromise between achieving optical transmission (as a result of previous ray tracing results) and overall size (footprint) of the light guide. Distal curves were specified with a radius of 70 mm and angle of 35°, while proximal curves were specified with a radius of 100 mm and angle of 37°. The larger proximal curves and the smaller distal curves allowed reduced converging angles among branches. The resulting alpha light guide design was constructed in CAD (Autodesk Inventor, Autodesk Inc.) and imported into TracePro for analysis. Ray trace modeling of the final alpha light guide design resulted in optical transmission ranging from 11% transmission for selected middle branches to 49% transmission for outer branches. At the conclusion of the alpha phase modeling, a prototype alpha phase light guide was manufactured by Apollo Optical Systems, Inc. An injection mold was constructed and the light guide produced from optical grade acrylic according to the design specifications of the CAD drawing. The alpha phase light guide was then evaluated using bench testing and subsequently incorporated into a prototype spectral illuminator for coupling to a fiber-based endoscope, as described below.

3.2. *Benchtop testing prototype*

A proof-of-concept spectral light source was designed to evaluate the ability of the multifurcated light guide to combine optical output from an array of λLEDs to a common output that could be coupled to the illumination fiber of a commercial endoscope. Benchtop testing included evaluation of the optical transmission of the multifurcated light guide, the transmission of the light guide + endoscope assembly and acquiring initial feasibility image data. Radiant flux and transmittance were measured for each λLED of the system, as well as through the alpha phase multifurcated light guide, and through the light guide + endoscope. Irradiance measurement stability (repeatability) was verified at 3 λLEDs by repeating measurements 5 times, with a complete system restart between each test. The coefficient of variation for each λLED ranged from 0.0015 to 0.0041, indicating high repeatability. The λLED-based spectral light source + endoscope was then used to acquire test images of swine colon. Test images included spectral reflectance and fluorescence (tissue autofluorescence) modalities (Fig. 5).

Benchtop testing resulted in a relatively low optical transmission through the light guide (0.01% to 4.37% depending on branch). Coupling through the endoscope illumination fiber resulted in additional transmission loss of 2-4% (these losses are in line with expected transmission efficiencies through an endoscope illumination fiber). As an example, the raw output of the 670 nm λLED achieved a peak spectraradiometric flux of ~2400 mW/cm^2 nm (Fig. 5(A)), while the power when transmitted through the light guide was ~60 mW/cm^2 nm and the power when transmitted through the light guide + endoscope was ~12 mW/cm^2 nm (Fig. 5(C)). The
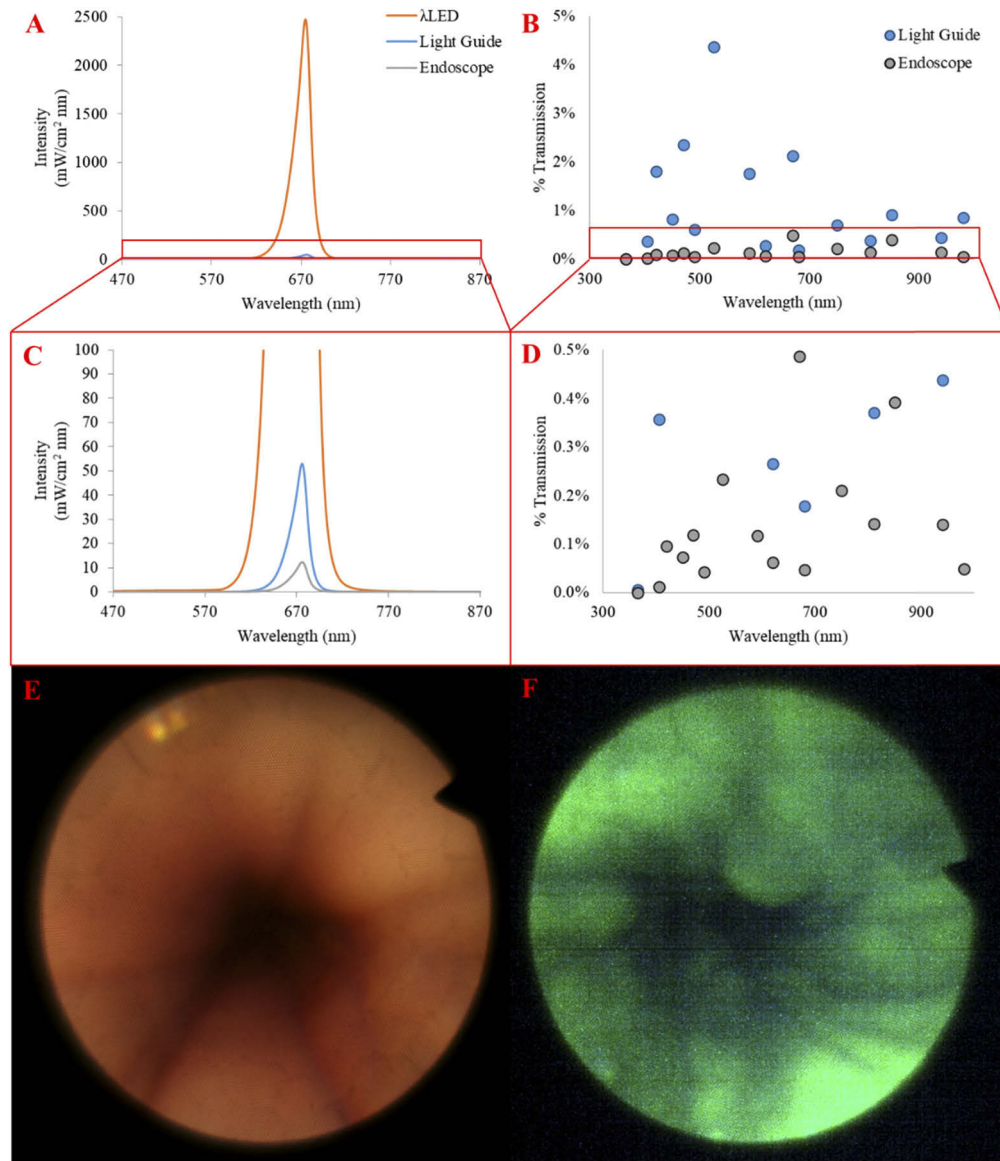
Fig. 5. Results from benchtop testing the proof-of-concept light source for spectral LED (λLED). (A) The spectraradiometric power of the 670 nm LED measured as the raw λLED, as transmitted through the light guide and as transmitted through the light guide + endoscope assembly. (B) The illumination % transmission for each λLED through the light guide as seen in Fig. 3(B) and through the light guide + endoscope. The subtrahend from these data would be the losses through the light guide and endoscope respectively. (C) Irradiance data from panel A rescaled to highlight the light guide and endoscope curves. (D) Transmission from panel B rescaled to highlight the lower transmission through the endoscope. The 365 nm LED did not transmit through the endoscope likely due to poor transmission through the illumination fiber. (E) An example false-colored reflectance spectral image stack and (F) a false-colored autofluorescence spectral image stack. Images false-colored according to wavelength using NIS Elements software (Nikon Elements).

transmitted light was measured through the light guide for each λLED in the set array and through the light guide + endoscope providing the output of the given λLED-branch combinations for the current prototype assembly (Fig. 5(B,D)). The 365 nm LED did not transmit through this system. The assumption is that the filters and fiber material of the endoscope block any UV light from transmitting to the colorectum to minimize radiation damage. This longer UV wavelength LED was selected in the prototype's array to test a wide selection of λLEDs for throughput and potential utility for fluorescence imaging by exciting known endogenous fluorescent tissue components (i.e. collagen, elastin or FAD) [41–43,52]. Due to the injection-molded nature of the solid light guide (i.e., manufactured as a single optical component), it was not possible to experimentally measure optical loss or percent transmission changes that occurred as a result of light guide branching at the branch points. However, ray trace simulations indicate that branch points have a compounding effect of optical losses, with each branch point contributing a similar fractional transmission loss. Also, it should be noted that curvature of the endoscope itself could result in some small losses and to minimize this variable from the experiments the endoscope was held straight for each test. In future work, light losses through the endoscope as a result of curvature will also be investigated [53,54].

Preliminary feasibility tests were also conducted using the spectral endoscope to image excised sections of swine colon. The power output of each λLED was adjusted in order to achieve a uniform spectral illumination profile. In order to achieve a specified power output for each wavelength, some scenarios only illuminated a subset of λLEDs available in order to provide the specified power to the endoscope tip. Therefore, the test images shown in Fig. 5(E-F) used a reduced number of wavelengths in order to achieve a flat spectral illumination profile. A reflectance spectral image stack was acquired (Fig. 5(E)) using λLEDs from 450 nm to 940 nm (12 λLEDs) at 0.3 mW illumination power and 100 ms integration time (1.2 s per image stack). If the full λLED array were used it would take 1.6 s for a reflectance image stack at 100 ms per wavelength band. One aspect to note is the green and blue channels provided enhanced contrast of vascular structures, similar to NBI (better seen in Appendix Figs. 8 and 9). The fluorescence spectral image stack (Fig. 5(F)) used 3 λLEDs (420 nm, 470 nm and 525 nm) at 0.3 mW, exciting fluorescence at wavelengths below the 560 nm emission filter cutoff. Spectral images were acquired at 10 seconds (30 s per image stack) to allow sufficient signal integration. This current setup could acquire a full fluorescence image stack in 160 s (2.67 min) if all 16 λLEDs excited the FOV and the respective emission spectra was filtered to the detector. All images were false-colored by wavelength using NIS Elements software (Nikon Instruments). The power and acquisition times used for this initial feasibility test represent tradeoffs between imaging speed and sensitivity as a result of the relatively low transmission of the alpha phase light guide and 0.3 mW of illumination power. Images were acquired at the acquisition times stated above to provide the current optimal spatial resolution in an image (purely the qualitative best image acquired) and sample reflectance videos were captured with varied acquisition speeds to prioritize framerate with a distinguishable field of view (current optimum is 8 fps). It should be noted that we were not acquiring or detecting colorectal cancer in these samples, purely spectral imagery examples using an endoscope.

While the alpha phase prototype was sufficient to demonstrate proof-of-principle operation and allow acquisition of initial image datasets, the optical power available at the endoscope tip was low, resulting in poor signal-to-noise ratios (SNR) in the acquired images, especially when operating in fluorescence modality (Fig. 5(F)). Upon comparison between the optical transmission of the simulation (11% - 49%) and the physical prototype (0.01% - 4.37%), it became clear that a return to the computational ray trace software was required to both refine the accuracy of the model and to evaluate alternative design geometries in an effort to increase transmission efficiency. Within the TracePro environment, the light guide material was updated from plexiglass to optical acrylic. In addition, the λLED was updated from the initial Cree 527 nm LED to a Marubeni 525 nm LED.

Finally, the interrogation plane (detection surface) was resized to match the input fiber bundle of an endoscope (5 mm diameter instead of 50 mm) and moved closer to the output of the light guide (2 mm between instead of 50 mm). These changes resulted in transmission of 3.9% in simulation for the 525 nm LED, which better coincides with the measured 2.1% transmission from benchtop testing. The light loss with this proof-of-concept spectral light source is significant and does not currently allow for the real-time excitation-scanning hyperspectral imaging goal. However, with the resulting transmission and the test images shown, it can be inferred that with adequate optical throughput we can achieve our excitation-scanning goals.

3.3. *Beta light guide models*

The benchtop testing of the alpha phase prototype was sufficient for demonstrating initial feasibility of the excitation-scanning approach in an endoscopic scenario, but did not provide sufficient illumination power necessary to achieve quality SNR fluorescence images (Fig. 5(D)). However, construction of the prototype system did provide an opportunity for model validation, revision of model parameters to better match real-world operation and revision of specifications for the desired end product. A beta light guide was next modeled using revised model parameters. Tier 1 & 2 ray tracing simulations reassessed the alpha phase modeling using these revised parameters and constraints. Results were consistent with the alpha phase models (Table 5).

For beta phase models, optical transmission increased with increasing lightpipe diameter, achieving a maximum of 86% with diameters of 8 mm or larger. Optical transmission also increased for decreasing lightpipe length. However, even for long lightpipes (>100 mm) a minimum transmission of 72% was achieved. Curved lightpipes were defined as a function of the radius and angle of a circumscribed arc. All angle values tested (15° – 90°, in increments of 15°) resulted in an increase of transmission with increasing arc radius to a maximum transmission of ~50% for arc radii ≥ 100 mm. Double curved lightpipes exhibited no transmission differences from a single curved lightpipe. Bifurcated lightpipes (e.g., merging two single curved lightpipes) were defined by the arc angle and radius of the two branches. Of note, in the case of merging two curved lightpipes, the overlapping area of the lightpipes (at the intersection) is also a function of the arc angle and radius of the lightpipes. Results from the bifurcated models indicated that the primary parameter regulating optical transmission was the arc radius, where a larger arc radius resulted in increased optical transmission, with a maximum of 35% achieved for an arc radius of ≥200 mm. The merger of a straight lightpipe with a curved lightpipe was also simulated. In this case, comparable lightpipe lengths were used for both branches (i.e., the length of the straight section was specified as equal to the arc length of the curved section). Results were similar to the results of merging two curved lightpipes. Hence, we can conclude that a similar transmission efficiency is achieved for the merger of two branches, regardless of whether two curved branches are merged or a curved branch and a straight branch are merged. Finally, lightpipe spacing was tested to see if it affected the internal reflection of light rays at the bifurcation points (i.e., reducing refraction and increasing transmission). For each distance between branches that was tested, one branch was illuminated while the output flux was measured at the common output and at the adjacent branch(es) to assess back illumination. Branch spacing had no effects on the transmission throughput (i.e., the transmission was approximately the same for each branch illuminated regardless of the distance between adjacent branches) and back illumination of adjacent branches was negligible.

Using the revised parameter values to more accurately account for real-life optical properties resulted in lower optical transmission for most of the beta phase models, when compared to similar alpha phase models. Two key factors likely contributed to reduced transmission: a change in viewing angle of the λLED and a revised diameter and placement of the interrogation plane. First, the λLED used for the alpha phase simulations (C503B-BAS/BAN/GAS/GAN, Cree) had an optical power output of 10 mW and a full viewing angle of 15°, while the λLED used for the

beta phase simulations (SMB1N-525V-02, Marubeni) had an optical power output of 230 mW and a full viewing angle of 22°. Hence, while the total power output of the beta phase λLED was much higher, the optical output was also more diffuse, leading to decreased efficiency when propagating through the solid light guide This was likely due to the inability to maintain total internal reflectance (TIR) within the light guide. Second, the alpha phase simulations measured radiant flux using an interrogation plane that was large (50 mm in diameter) and placed at a long distance from the exit of the light guide (50 mm) to ensure that the far-field illumination profile was measured. Transmission was calculated using the output flux from the light guide divided by the total input flux of the λLED. By contrast, the beta phase simulations utilized a much smaller interrogation plane that matched the diameter of the endoscope illumination fiber (5 mm) and was placed at a distance similar to the illumination fiber placement when coupling the solid light guide to the endoscope (2 mm). This would alter the measurements as the former tests did not account for exiting the lightpipe/light guide and the change in refractive indices. Even though it is a 2 mm difference, the energy change could account for a change in transmission results in the beta tests. Hence, while the optical transmission values predicted by the beta phase models in Tiers 1 and 2 of testing were lower than corresponding alpha phase models, they are much closer to the actual values encountered when constructing the physical prototype.

Tier 3 testing produced 4 versions of a multifurcated solid light guide: two symmetrical designs and two wave-shaped designs (Fig. 4). The symmetrical models utilized design aspects of the alpha prototype solid light guide and would require minimal redesign of the overall spectral light source. However, the simulation results from Symmetrical Design 1 indicated that multiple merge points in the light guide reduced the transmission (Fig. 4(D)). Symmetrical Design 2 minimized the number of merge points to mitigate light losses (Fig. 4(F)). Finally, a wave-shaped light guide was designed to create one merging point and manipulate the light in the same direction for every branch. The wave-shape was created in two configurations: Wave Design 1 with spacing between branches created by adding straight lengths of lightpipe between curves (Fig. 4(H)) and Wave Design 2 with increasing arc radius for each branch (Fig. 4(I)). For all Tier 3 beta phase simulations, the optical power was measured at each branch point in order to assess the source of optical transmission losses throughout the light guide.

Results from Symmetrical Design 1 (Fig. 4(A-D)), with 2, 4, 8 or 16 branches, demonstrate that doubling the number of merge points reduces the transmission by ~50% (Fig. 6(A)). Only the 2 and 4 branch models met the optical performance requirements of ≥ 10% transmission. However, this 4-branch model would provide an insufficient number of wavelengths to acquire a spectral image stack. To investigate the effects of reducing the number of merge points while maintaining the number of branches, Symmetrical Design 2 was developed (Fig. 4(E-F)), which featured either 4 or 16 branches, but with merge points located in close proximity and with some of the branches passing straight into the merge point instead of along an arc. However, generating one larger merge point instead of 2 separate merge points provided reduced transmission for many of the branches (Fig. 6(B)). The reduced performance is likely due to the complex geometry formed when multiple branches merge in close proximity and likely to the presence of straight branches, leading to ray-substrate angles outside of the critical angle. To further investigate the utility of using an arc geometry and maintaining tangent criteria at merge points, an additional set of wave-shaped light guides were developed (Fig. 4(G-I)). Wave Design 1 was created to maintain the same direction of curvature for either 8 (Fig. 4(G)) or 16 (Fig. 4(H)) branches. Model results (Fig. 6(C)) indicated an increase in transmission, but also a wide variability in transmission from branch to branch (between 0-30% for the 16-branch version). To further improve transmission, Wave Design 2 was created using parabolic geometry for the curved branches (Fig. 4(I)). Results (Fig. 6(D)) demonstrated a range of optical transmission between 4-20%, depending on the branch. However, by coupling high power output λLEDs to low transmission branches and low

power output λLEDs to high transmission branches, it is possible to meet the specified power of 10 mW per branch.
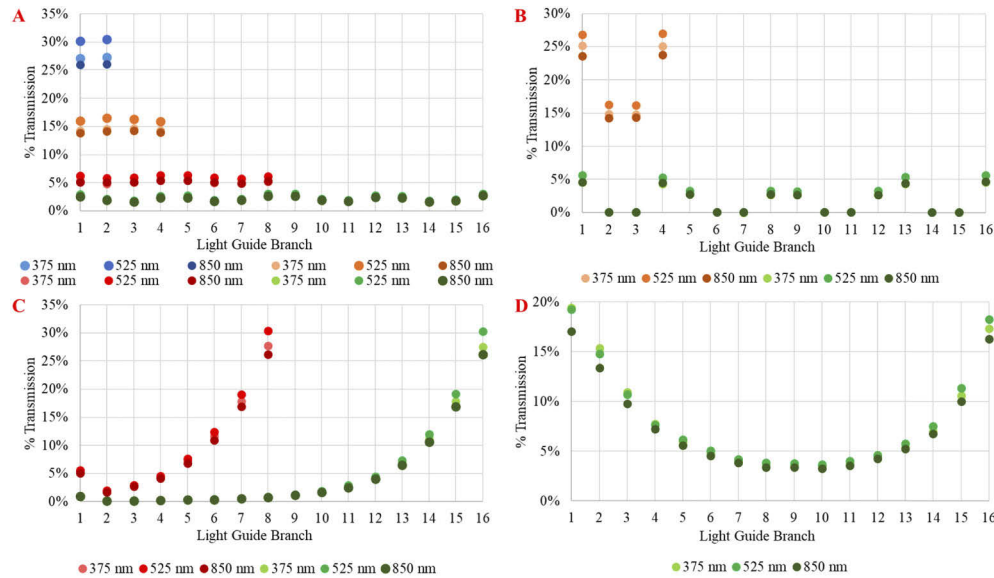

Fig. 6. Results of the ray tracing simulations for the beta light guide models showing optical transmission as a function of % transmission vs. branch illuminated. (A) Results of the Symmetrical Design 1 (Fig. 4(A-D)) transmitting LED light per branch for a 2 (blue), 4 (orange), 8 (red) and 16 (green) branch model over the range of LEDs. A UV, visible and IR LED was graphed to show any throughput changes as a result of wavelengths. (B) Results of Symmetrical Design 2 transmitting (Fig. 4(E-F)) LED light per branch for a 4 and 16 branch model over the range of LEDs. (C) Results of the Wave Design 1 (Fig. 4(G-H)) transmitting LED light per branch for an 8 and 16 branch model over the range of LEDs. (D) Results of Wave Design 2 (Fig. 4(I)) transmitting LED light per branch for a 16-branch model over the range of LEDs.

3.3.1. Comparison of ray trace to requirements

The overall goal of this work was to develop a novel geometry of multifurcated optical light guide that could meet the requirements of 10 mW of power per branch, create a flat spectral response and produce an illumination beam with similar numerical aperture to the endoscope fiber bundle. While initial feasibility of the approach was demonstrated using the alpha phase modeling and prototyping efforts, benchtop testing revealed that further work was needed to meet the illumination power requirements in order to achieve quality SNR endoscopic image data at video-rate acquisition. The beta phase modeling efforts were then performed, with results indicating that a 16-branch geometry, Wave Design 2 (Fig. 4(I)) could provide between 4-20% optical transmission (Fig. 6(D)), depending on branch. To demonstrate the theoretical feasibility of this revised geometry for achieving spectral illumination, a λLED and light guide combination was modeled that coupled high power output λLEDs (see Table 3 and Fig. 7(A) for λLED power and transmission requirements) to low transmission branches of Wave Design 2 and low power output λLEDs to high transmission branches of Wave Design 2, simulating the spectral output to the endoscope (Fig. 7).

Results from specific λLED-branch combinations of the optical raytrace model simulation indicate that it is possible to achieve the required 10 mW (and higher to the desired 20 mW) of power per λLED based on the transmission efficiency (Fig. 7(B)) and the conversion to expected
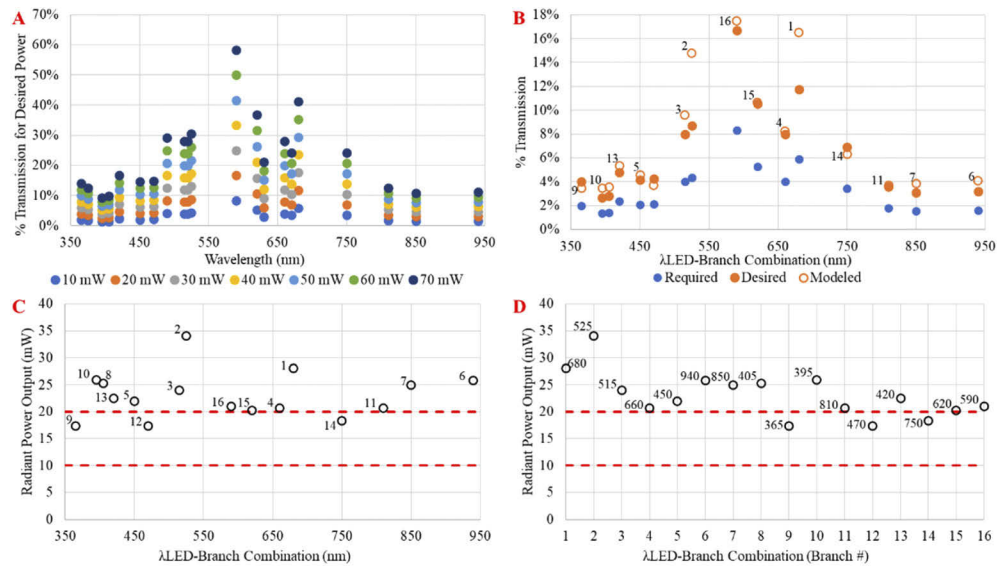
Fig. 7. Comparison of the required outputs of each λLED to the theoretical output of the simulation model Wave Design 2 in Fig. 4(I). (A) The % transmission per λLED needed to achieve a set power output from Table 3. (B) The data for wavelength transmission of 10 mW (Required – shown as solid blue circles) and 20 mW (Desired – solid orange circles) from panel A compared to the transmission of the λLED-branch combination determined using the results of the Wave Design 2 light guide seen in Fig. 4(I) (Modeled – open orange circles). Branch #'s which each LED should be coupled with are labeled above each open, orange data point. A reduced number of wavelengths (from 21 available and reduced to 16 positions of the multifurcated light guide) was selected to allow a range of comparable excitation wavelengths observed in literature. (C) Conversion of panel B to expected radiant power output through the Wave Design 2 in Fig. 4(I) with branches labeled above each wavelength (x-axis) data point. The 10 mW required and 20 mW desired levels are denoted with dashed red lines. (D) The data from panel D reorganized in the linear branch order (x-axis) of the multifurcated light guide while the labels represent the wavelength of each branch. Dashed red lines remain for the 10 mW and 20 mW thresholds.

power outputs (Fig. 7(C-D)). The comparison shows the model has 3 λLED-branch combinations that are less than the desired 20 mW optical power output. As seen in Table 6 the λLED array would not be in increasing wavelength order, but this is inconsequential as the λLEDs can be illuminated in any order specified through the use of the corresponding TTL control signals.

The proof-of-concept λLED-based spectral endoscopic system (Fig. 3), which produced an irradiance output maximum of 2.6 mW of power (of the 670 nm λLED seen in Fig. 5(B,D)), acquired a reflectance image stack (Fig. 5(E)) in 1.2 s and a fluorescence image stack (Fig. 5(F)) in 30 s. The simulation data for an optimized solution of the multifurcated solid light guide illustrates the Wave Design 2 (seen in Fig. 4(I)) with the right λLED-branch coupling could potentially provide an average of 20 mW irradiance power to the endoscope. Assuming loss through the endoscope to an extreme of 15 mW irradiance at the output of the endoscope still meets the required output of 10 mW and would have at least 5X more illumination than the current physical prototype. This irradiance increase infers that the acquisition time for an image stack (reflectance, fluorescence or a mixture) should decrease to speeds for video-rate hyperspectral endoscopy.

Table 6. Tabulated data from Fig. 7 comparing the required (Column 2) and desired (Column 3) transmission of each λLED (from Table 3) to the simulated (Column 4) transmission results (also plotted in Fig 6(D)). The corresponding radiant power potential (mW) for each λLED (Column 5) and the mount of power over or under (±) the 10 mW required and 20 mW desired thresholds were also assessed (Column 6). λLED and corresponding multifurcated light guide branch number combinations can be seen by comparing Columns 1 and 7.

LED (nm)	Required (10mW) Transmission	Desired (20mW) Transmission	Modeled Transmission	Radiant Power Output (mW)	(± to 10mW/± to 20mW)	Corresponding Branch
365	2%	4%	3.5%	17.3	(+7.3/-2.7)	9
395	1%	3%	3.5%	25.9	(+15.9/+5.9)	10
405	1%	3%	3.6%	25.3	(+15.3/+5.3)	8
420	2%	5%	5.4%	22.5	(+12.5/+2.5)	13
450	2%	4%	4.6%	21.9	(+11.9/+1.9)	5
470	2%	4%	3.7%	17.3	(+7.3/-2.7)	12
515	4%	8%	9.6%	24.0	(+14.0/+4.0)	3
525	4%	9%	14.8%	34.0	(+24.0/+14.0)	2
590	8%	17%	17.5%	21.0	(+11.0/+1.0)	16
620	5%	11%	10.7%	20.2	(+10.2/+0.2)	15
660	4%	8%	8.3%	20.6	(+10.6/+0.6)	4
680	6%	12%	16.5%	28.0	(+18.0/+8.0)	1
750	3%	7%	6.3%	18.3	(+8.3/-1.7)	14
810	2%	4%	3.7%	20.6	(+10.6/+0.6)	11
850	2%	3%	3.8%	25.0	(+15.0/+5.0)	7
940	2%	3%	4.1%	25.8	(+15.8/+5.8)	6

4. Future work

Multifurcated solid light guides, coupled to discrete wavelength LEDs (λLEDs) represent a novel approach for providing spectral illumination with high switching speeds. In this work, we have shown the feasibility of using this novel approach through alpha model simulations and prototyping, followed by verification through benchtop testing. Furthermore, the results of physical testing provided insight for optimization and the subsequent beta model simulations. Future work will focus on prototype development of the final optimized light guide geometry (Fig. 4(I)), benchtop testing and endoscope integration. Additional system variations will also be investigated, such as the use of coupling lenses for λLED collimation prior to light guide coupling, manipulation of the light guide entrance geometry for improved TIR and techniques for light guide-endoscope coupling to match numerical aperture requirements. Endoscope testing will focus on feasibility demonstration in excised tissues and *in vivo* animal models with a long-term goal to transition the technology to a clinical platform for clinical pilot testing. If successful, this technology may represent the next step in developing endoscope systems with enhanced contrast for clinical screening.
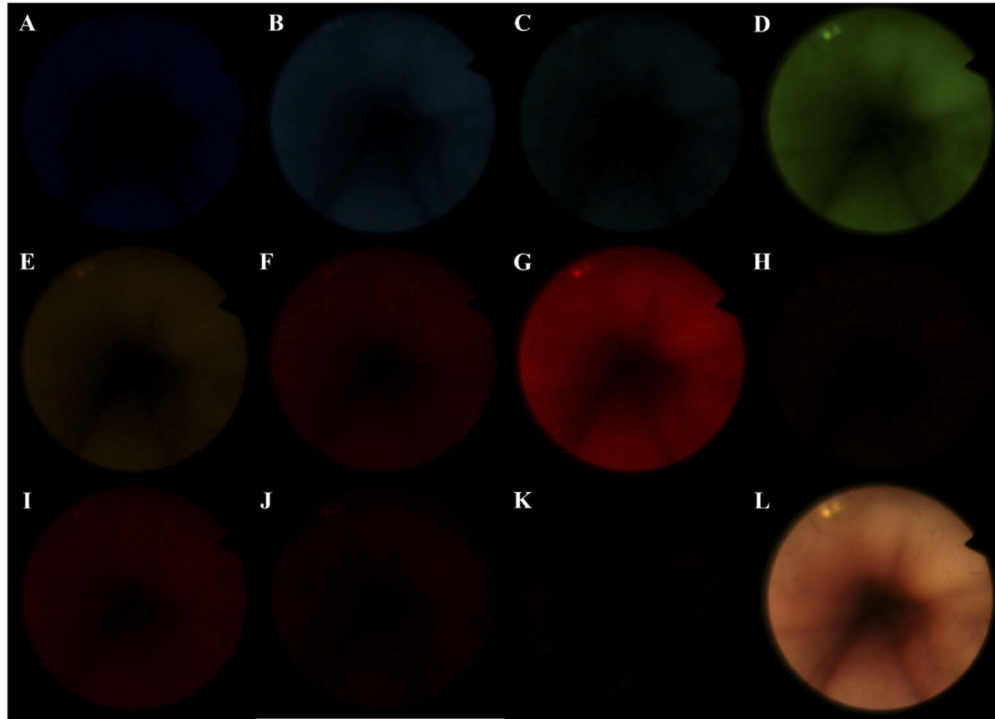
Fig. 8. Image data corresponding to Fig. 5(E) where reflectance spectral images have been divided by wavelength band and false colored for visualization. The channels are presented in respective wavelength order: (A) 450 nm, (B) 470 nm, (C) 490 nm, (D) 525 nm, (E) 590 nm, (F) 620 nm, (G) 670 nm, (H) 680 nm, (I) 750 nm, (J) 810 nm, (K) 850 nm and (L) the overlayed image as seen in Fig. 5(E). The 940 nm channel was omitted due to indiscernible signal and increased noise collected. False-coloring was applied using the wavelength coloring function in NIS Elements software; hence the near-infrared wavelengths have all been false-colored at the maximum wavelength (800 nm) available. Each channel look up table (LUT) was uniformly scaled to increase intensity while displaying which channels produced a higher reflectance signal.
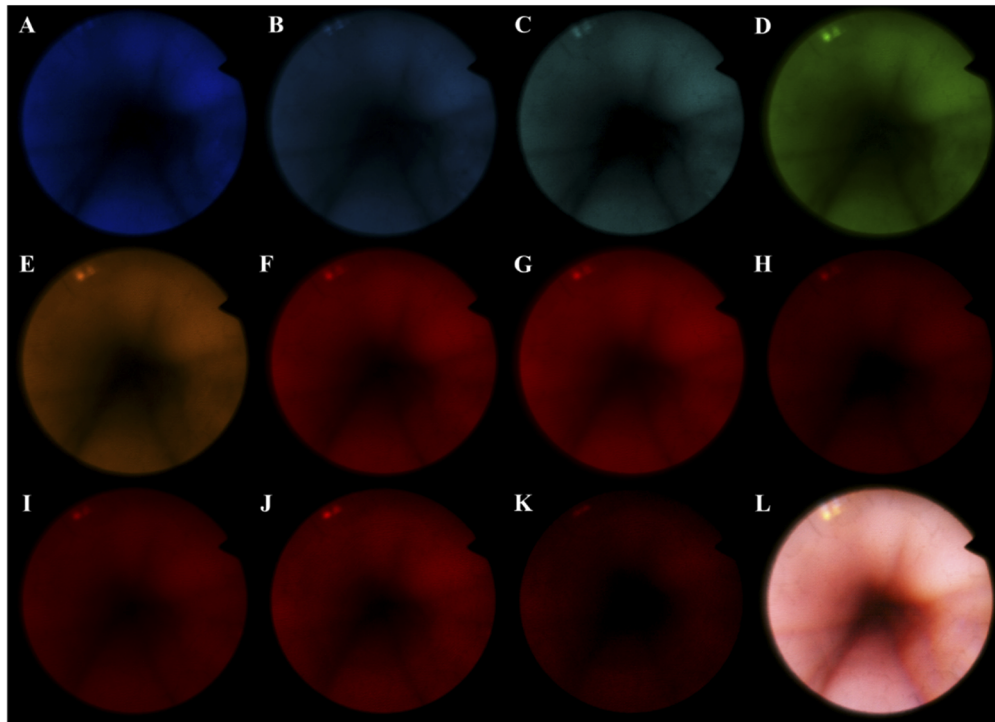
Fig. 9. Data from Fig. 8 and corresponding Fig. 5(E), where the look-up table for each wavelength band has been scaled independently. The channels are presented in respective wavelength order: (A) 450 nm, (B) 470 nm, (C) 490 nm, (D) 525 nm, (E) 590 nm, (F) 620 nm, (G) 670 nm, (H) 680 nm, (I) 750 nm, (J) 810 nm, (K) 850 nm and (L) the overlayed image as seen in Fig. 5(E). The 940 nm channel was omitted due to indiscernible signal and increased noise collected. False-coloring was applied using the wavelength coloring function in NIS Elements software; hence the near-infrared wavelengths have all been false-colored at the maximum wavelength (800 nm) available. Channel look up tables (LUT) were individually scaled to display each channel for visual clarity (i.e., the min and max intensity levels to map to the color look-up table were adjusted on a per-channel basis to enhance visualization of each channel). Enhanced contrast can be seen by vasculature in the blue and green channels.

Funding

Acknowledgements

Disclosures

The corresponding author, Dr. Leavesley, is named as an inventor on a patent (US patent no. 10,393,964 B2) issued to the University of South Alabama for the novel design of the multibranched optical light guide (P). Drs. Leavesley and Rich disclose financial interest in a start-up company, SpectraCyte LLC, founded to commercialize spectral imaging technologies (I).

References

1. "Definition of -SCOPY," https://www.merriam-webster.com/dictionary/-scopy.
2. R. L. Siegel, K. D. Miller, and A. Jemal, "Cancer statistics, 2017," Ca-Cancer J. Clin. **67**(1), 7–30 (2017).
3. R. L. Siegel, K. D. Miller, and A. Jemal, "Cancer statistics, 2019," Ca-Cancer J. Clin. **69**(1), 7–34 (2019).
4. D. K. Rex, C. S. Cutler, G. T. Lemmel, E. Y. Rahmani, D. W. Clark, D. J. Helper, G. A. Lehman, and D. G. Mark, "Colonoscopic miss rates of adenomas determined by back-to-back colonoscopies," Gastroenterology **112**(1), 24–28 (1997).
5. T. Kaltenbach, S. Friedland, and R. Soetikno, "A randomised tandem colonoscopy trial of narrow band imaging versus white light examination to compare neoplasia miss rates," Gut **57**(10), 1406–1412 (2008).
6. R. Higashi, T. Uraoka, J. Kato, K. Kuwaki, S. Ishikawa, Y. Saito, T. Matsuda, H. Ikematsu, Y. Sano, S. Suzuki, Y. Murakami, and K. Yamamoto, "Diagnostic accuracy of narrow-band imaging and pit pattern analysis significantly improved for less-experienced endoscopists after an expanded training program," Gastrointest. Endosc. **72**(1), 127–135 (2010).
7. A. Ignjatovic, S. Thomas-Gibson, J. E. East, A. Haycock, P. Bassett, P. Bhandari, R. Man, N. Suzuki, and B. P. Saunders, "Development and validation of a training module on the use of narrow-band imaging in differentiation of small adenomas from hyperplastic colorectal polyps," Gastrointest. Endosc. **73**(1), 128–133 (2011).
8. S. J. Chung, D. Kim, J. H. Song, H. Y. Kang, G. E. Chung, J. Choi, Y. S. Kim, M. J. Park, and J. S. Kim, "Comparison of detection and miss rates of narrow band imaging, flexible spectral imaging chromoendoscopy and white light at screening colonoscopy: a randomised controlled back-to-back study," Gut **63**(5), 785–791 (2014).
9. E. H. van der Heijden, W. Hoefsloot, H. W. van Hees, and O. C. Schuurbiers, "High definition bronchoscopy: a randomized exploratory study of diagnostic value compared to standard white light bronchoscopy and autofluorescence bronchoscopy," Respir. Res. **16**(1), 33 (2015).
10. M. Andolfi, R. Potenza, R. Capozzi, V. Liparulo, F. Puma, and K. Yasufuku, "The role of bronchoscopy in the diagnosis of early lung cancer: a review," J. Thorac. Dis. **8**(11), 3329–3337 (2016).
11. W. Chen, X. Gao, Q. Tian, and L. Chen, "A comparison of autofluorescence bronchoscopy and white light bronchoscopy in detection of lung cancer and preoneoplastic lesions: a meta-analysis," Lung Cancer **73**(2), 183–188 (2011).
12. A. Ignjatovic, J. East, T. Guenther, J. Hoare, J. Morris, K. Ragunath, A. Shonde, J. Simmons, N. Suzuki, and S. Thomas-Gibson, "What is the most reliable imaging modality for small colonic polyp characterization? Study of white-light, autofluorescence, and narrow-band imaging," Endoscopy **43**(02), 94–99 (2011).
13. H.-M. Chiu, C.-Y. Chang, C.-C. Chen, Y.-C. Lee, M.-S. Wu, J.-T. Lin, C.-T. Shun, and H.-P. Wang, "A prospective comparative study of narrow-band imaging, chromoendoscopy, and conventional colonoscopy in the diagnosis of colorectal neoplasia," Gut **56**(3), 373–379 (2007).
14. F. Asano, "Advanced bronchoscopy for the diagnosis of peripheral pulmonary lesions," Respir. Investig. **54**(4), 224–229 (2016).
15. K. Togashi, H. Osawa, K. Koinuma, Y. Hayashi, T. Miyata, K. Sunada, M. Nokubi, H. Horie, and H. Yamamoto, "A comparison of conventional endoscopy, chromoendoscopy, and the optimal-band imaging system for the differentiation of neoplastic and non-neoplastic colonic polyps," Gastrointest. Endosc. **69**(3), 734–741 (2009).

16. R. Sato, M. Fujiya, J. Watari, N. Ueno, K. Moriichi, S. Kashima, S. Maeda, K. Ando, H. Kawabata, and R. Sugiyama, "The diagnostic accuracy of high-resolution endoscopy, autofluorescence imaging and narrow-band imaging for differentially diagnosing colon adenoma," Endoscopy **43**(10), 862–868 (2011).

17. T. Matsumoto, M. Esaki, R. Fujisawa, S. Nakamura, T. Yao, and M. Iida, "Chromoendoscopy, narrow-band imaging colonoscopy, and autofluorescence colonoscopy for detection of diminutive colorectal neoplasia in familial adenomatous polyposis," Dis. Colon Rectum **52**(6), 1160–1165 (2009).

18. D. J. Mulla, "Twenty five years of remote sensing in precision agriculture: Key advances and remaining knowledge gaps," Biosyst. Eng. **114**(4), 358–371 (2013).

19. W. S. Lee, V. Alchanatis, C. Yang, M. Hirafuji, D. Moshou, and C. Li, "Sensing technologies for precision specialty crop production," Comput. Electron. Agric. **74**(1), 2–33 (2010).

20. R. M. Cavalli, F. Colosi, A. Palombo, S. Pignatti, and M. Poscolieri, "Remote hyperspectral imagery as a support to archaeological prospection," J. Cult. Herit. **8**(3), 272–283 (2007).

21. R. M. Cavalli, G. A. Licciardi, and J. Chanussot, "Detection of anomalies produced by buried archaeological structures using nonlinear principal component analysis applied to airborne hyperspectral image," IEEE J. Sel. Top. Appl. Earth Obs. Remote Sens. **6**(2), 659–669 (2013).

22. D.-W. Sun, *Hyperspectral Imaging for Food Quality Analysis and Control* (Elsevier, 2010).

23. P. Talens, L. Mora, N. Morsy, D. F. Barbin, G. ElMasry, and D.-W. Sun, "Prediction of water and protein contents and quality classification of Spanish cooked ham using NIR hyperspectral imaging," J. Food Eng. **117**(3), 272–280 (2013).

24. D. Goltz, M. Attas, G. Young, E. Cloutis, and M. Bedynski, "Assessing stains on historical documents using hyperspectral imaging," J. Cult. Herit. **11**(1), 19–26 (2010).

25. S. J. Kim, S. Zhuo, F. Deng, C.-W. Fu, and M. Brown, "Interactive visualization of hyperspectral images of historical documents," IEEE Trans. Vis. Comput. Graph. **16**(6), 1441–1448 (2010).

26. S. V. Panasyuk, S. Yang, D. V. Faller, D. Ngo, R. A. Lew, J. E. Freeman, and A. E. Rogers, "Medical hyperspectral imaging to facilitate residual tumor identification during surgery," Cancer Biol. Ther. **6**(3), 439–446 (2007).

27. K. J. Zuzak, R. P. Francis, E. F. Wehner, M. Litorja, J. A. Cadeddu, and E. H. Livingston, "Active DLP Hyperspectral Illumination: A Noninvasive, in Vivo, System Characterization Visualizing Tissue Oxygenation at Near Video Rates," Anal. Chem. **83**(19), 7424–7430 (2011).

28. S. Ortega, H. Fabelo, D. K. Iakovidis, A. Koulaouzidis, and G. M. Callico, "Use of hyperspectral/multispectral imaging in gastroenterology. Shedding some–different–light into the dark," J. Clin. Med. **8**(1), 36 (2019).

29. G. Lu and B. Fei, "Medical hyperspectral imaging: a review," J. Biomed. Opt. **19**(1), 010901 (2014).

30. J. Lin, N. T. Clancy, J. Qi, Y. Hu, T. Tatla, D. Stoyanov, L. Maier-Hein, and D. S. Elson, "Dual-modality endoscopic probe for tissue surface shape reconstruction and hyperspectral imaging enabled by deep neural networks," Med. Image Anal. **48**, 162–176 (2018).

31. M. E. Martin, M. B. Wabuyele, K. Chen, P. Kasili, M. Panjehpour, M. Phan, B. Overholt, G. Cunningham, D. Wilson, and R. C. DeNovo, "Development of an advanced hyperspectral imaging (HSI) system with applications for cancer detection," Ann. Biomed. Eng. **34**(6), 1061–1068 (2006).

32. R. T. Kester, N. Bedard, L. Gao, and T. S. Tkaczyk, "Real-time snapshot hyperspectral imaging endoscope," J. Biomed. Opt. **16**(5), 056005 (2011).

33. Z. Han, A. Zhang, X. Wang, Z. Sun, M. D. Wang, and T. Xie, "In vivo use of hyperspectral imaging to develop a noncontact endoscopic diagnosis support system for malignant colorectal tumors," J. Biomed. Opt. **21**(1), 016001 (2016).

34. S. Duraipandian, M. S. Bergholt, W. Zheng, K. Y. Ho, M. Teh, K. G. Yeoh, J. B. Y. So, A. Shabbir, and Z. Huang, "Real-time Raman spectroscopy for in vivo, online gastric cancer diagnosis during clinical endoscopic examination," J. Biomed. Opt. **17**(8), 081418 (2012).

35. A. Goto, J. Nishikawa, S. Kiyotoki, M. Nakamura, J. Nishimura, T. Okamoto, H. Ogihara, Y. Fujita, Y. Hamamoto, and I. Sakaida, "Use of hyperspectral imaging technology to develop a diagnostic support system for gastric cancer," J. Biomed. Opt. **20**(1), 016017 (2015).

36. H. Akbari, K. Uto, Y. Kosugi, K. Kojima, and N. Tanaka, "Cancer detection using infrared hyperspectral imaging," Cancer Sci. **102**(4), 852–857 (2011).

37. E. J. Baltussen, E. N. Kok, S. G. B. de Koning, J. Sanders, A. G. Aalbers, N. F. Kok, G. L. Beets, C. C. Flohil, S. C. Bruin, and K. F. Kuhlmann, "Hyperspectral imaging for tissue classification, a way toward smart laparoscopic colorectal surgery," J. Biomed. Opt. **24**(01), 1 (2019).

38. P. M. Schaefer, S. Kalinina, A. Rueck, C. A. F. von Arnim, and B. von Einem, "NADH Autofluorescence—A Marker on its Way to Boost Bioenergetic Research," Cytometry A **95**(1), 34–46 (2019).

39. C. C. Fjeld, W. T. Birdsong, and R. H. Goodman, "Differential binding of NAD+ and NADH allows the transcriptional corepressor carboxyl-terminal binding protein to serve as a metabolic sensor," Proc. Natl. Acad. Sci. **100**(16), 9202–9207 (2003).

40. H. L. Zhao, C. P. Zhang, H. Zhu, Y. F. Jiang, and X. B. Fu, "Autofluorescence of collagen fibres in scar," Skin Res. Technol. **23**(4), 588–592 (2017).

41. H. Puchtler, F. S. Waldrop, and L. S. Valentine, "Fluorescence microscopic distinction between elastin and collagen," Histochemie **35**(1), 17–30 (1973).

42. M. Fang, J. Yuan, C. Peng, and Y. Li, "Collagen as a double-edged sword in tumor progression," Tumour Biol. **35**(4), 2871–2882 (2014).

43. M. C. Skala, K. M. Riching, A. Gendron-Fitzpatrick, J. Eickhoff, K. W. Eliceiri, J. G. White, and N. Ramanujam, "In vivo multiphoton microscopy of NADH and FAD redox states, fluorescence lifetimes, and cellular morphology in precancerous epithelia," Proc. Natl. Acad. Sci. **104**(49), 19494–19499 (2007).

44. H.-T. Lim and V. M. Murukeshan, "A four-dimensional snapshot hyperspectral video-endoscope for bio-imaging applications," Sci. Rep. **6**(1), 1–10 (2016).

45. P. F. Favreau, J. A. Deal, D. A. Weber, T. C. Rich, and S. J. Leavesley, "Assessment of autofluorescent signatures in multiple tissue types with novel excitationscanning hyperspectral imaging," FASEB J. **30**(S1), 51.1 (2016).

46. P. F. Favreau, C. Hernandez, T. Heaster, D. F. Alvarez, T. C. Rich, P. Prabhat, and S. J. Leavesley, "Excitation-scanning hyperspectral imaging microscope," J. Biomed. Opt. **19**(4), 046010 (2014).

47. J. A. Deal, P. Favreau, D. Weber, T. Rich, and S. Leavesley, "Potential of Hyperspectral Imaging for Label-free Tissue and Pathology Classification," FASEB J. **30**(S1), 51.2 (2016).

48. J. Deal, S. Mayes, C. Browning, S. Hill, P. Rider, C. Boudreaux, T. C. Rich, and S. J. Leavesley, "Identifying molecular contributors to autofluorescence of neoplastic and normal colon sections using excitation-scanning hyperspectral imaging," J. Biomed. Opt. **24**(2), 1 (2018).

49. S. J. Leavesley, M. Walters, C. Lopez, T. Baker, P. F. Favreau, T. C. Rich, P. F. Rider, and C. W. Boudreaux, "Hyperspectral imaging fluorescence excitation scanning for colon cancer detection," J. Biomed. Opt. **21**(10), 104003 (2016).

50. R. Shrestha and J. Hardeberg, "Multispectral imaging using LED illumination and an RGB camera," *Color Imaging Conf.* (2013).

51. M. Parmar, S. Lansel, and J. Farrell, "An LED-based lighting system for acquiring multispectral scenes," Proc. SPIE **8299**, 82990P (2012).

52. J. Galbán, I. Sanz-Vicente, J. Navarro, and S. de Marcos, "The intrinsic fluorescence of FAD and its application in analytical chemistry: a review," Methods Appl. Fluoresc. **4**(4), 042005 (2016).

53. R. Morgan, J. S. Barton, P. G. Harper, and J. D. C. Jones, "Wavelength dependence of bending loss in monomode optical fibers: effect of the fiber buffer coating," Opt. Lett. **15**(17), 947 (1990).

54. M. van Eijkelenborg, J. Canning, T. Ryan, and K. Lyytikainen, "Bending-induced colouring in a photonic crystal fibre," Opt. Express **7**(2), 88 (2000).